ChemComm

ROYAL SOCIETY OF CHEMISTRY

COMMUNICATION

View Article Online
View Journal | View Issue

Cite this: *Chem. Commun.*, 2023, **59**, 2287

Received 22nd November 2022,
Accepted 27th January 2023

DOI: 10.1039/d2cc06316f

rsc.li/chemcomm

Direct electrochemical identification of rare microscopic catalytic active sites†

Cameron L. Bentley, *[a] Lachlan F. Gaudin [a] and Minkyung Kang [b]

Local voltammetric analysis with a scanning electrochemical droplet cell technique, in combination with a new data processing protocol (termed data binning and trinisation), is used to directly identify previously unseen regions of elevated electrocatalytic activity on the basal plane (BP) of molybdenum disulfide (2H-MoS_2). This includes BP-like structures with hydrogen evolution reaction activities approaching that of the edge plane and rare nanoscale electrocatalytic "hot-spots" present at an areal density of approximately 0.2–1 μm^{-2}. Understanding the nature of (sub)microscopic catalytic active sites, such as those identified herein, is crucial to guide the rational design of next-generation earth-abundant materials for renewable fuels production.

Molybdenum disulfide (MoS_2) and related transition metal dichalcogenides (TMDs) have attracted significant attention for their role as promising earth-abundant electrocatalysts for the hydrogen evolution reaction (HER) in (photo)electrochemical water-splitting.[1–4] Bulk molybdenite (2H-MoS_2) has a layered structure, and many studies have reported that the edge plane (EP) is solely responsible for HER electrocatalysis, with some authors going as far as calling the basal plane (BP) ''inert'' or ''not electroactive''.[5] More recently, high-resolution electrochemical imaging studies have debunked this hypothesis, demonstrating that while the EP is indeed highly active for the HER (directly visualised at few- to multi-layer step edge features), the BP also possesses non-negligible catalytic activity, with an exchange current density (j_0) of $\sim 3 \times 10^{-6}$ A cm^{-2} (*i.e.*, comparable to polycrystalline Au or Ni).[6] Since then, it has been demonstrated[7–9] that the BP activity can vary from surface-to-surface (or crystal-to-crystal), or even within a single BP on the μm-scale, but still always has relatively low activity relative to the EP ($j_0 \approx 10^{-4}$ A cm^{-2}, ref. 6). Expanding on these studies, this work reports on the first direct identification of the following on the BP of natural molybdenite (2H-MoS_2) crystals: (1) structures with local HER activities approaching that of the EP and (2) sub-μm (single-pixel) electrocatalytic ''hot-spots''.

Monocrystalline electrodes of *n*-type MoS_2 were prepared by mechanical exfoliation of a natural molybdenite crystal by the ''scotch tape method'', as previously reported.[6,10] The freshly cleaved electrodes are considered to be representative of the bulk material (*i.e.*, mm-size lateral dimensions, >100 μm thickness) and were probed for HER electrocatalytic activity using scanning electrochemical cell microscopy (SECCM).[11,12] Full experimental protocols are summarised in the ESI,† Section S1, but are described briefly here to assist with understanding. SECCM employs a fluidic nanopipette probe to carry out local electrochemical measurements (*e.g.*, voltammetry herein, but can be performed with any electrochemical perturbation in principle[13]) within a confined region of an electrode surface, at a spatial-resolution defined by the dimensions of droplet contact (tip radius and area of $\sim$0.067 μm and $\sim$0.014 μm^2 herein, see ESI,† Fig. S1 and S2).[14,15] Deploying SECCM in the voltammetric hopping-mode[16] allows for the construction of movies of spatially-resolved electrochemical activity, an example of which is shown in the ESI,† Movie S1. The maximum catalytic current (i_{max}) was extracted from these data at −1.13 V *vs.* SCE (details provided in the ESI,† Section S1) to construct the electrochemical map shown in Fig. 1a. An additional electrochemical map of potential required to achieve 10 mA cm^{-2} (E @ 10 mA cm^{-2}), constructed through exponential fitting of the i–E data (ESI,† Section S2 and Fig. S5), also reflected the same pattern of HER reactivity.

Comparison of Fig. 1a with the co-located topography map in Fig. 1b reveals that the scan area is made up of three regions of BP (labelled BP1–BP3 in Fig. 1b) separated by two multi-layer step edge features (labelled SE in Fig. 1b) of similar height (40–50 nm, see line scan data in the ESI,† Fig. S6). Note that the SECCM topography maps reported herein have a z-resolution on the order of the SECCM probe size (*i.e.*, $\sim$10 nm) and thus

---

[a] *School of Chemistry, Monash University, Clayton, Victoria 3800, Australia. E-mail: cameron.bentley@monash.edu*

[b] *Institute for Frontier Materials Deakin University, Burwood, Victoria 3125, Australia*

† Electronic supplementary information (ESI) available: Experimental section (Section S1); extended analysis of SECCM data (Section S2); additional SEM Images of the SECCM scan areas (Section S3) and movie captions (Section S4). See DOI: **https://doi.org/10.1039/d2cc06316f**

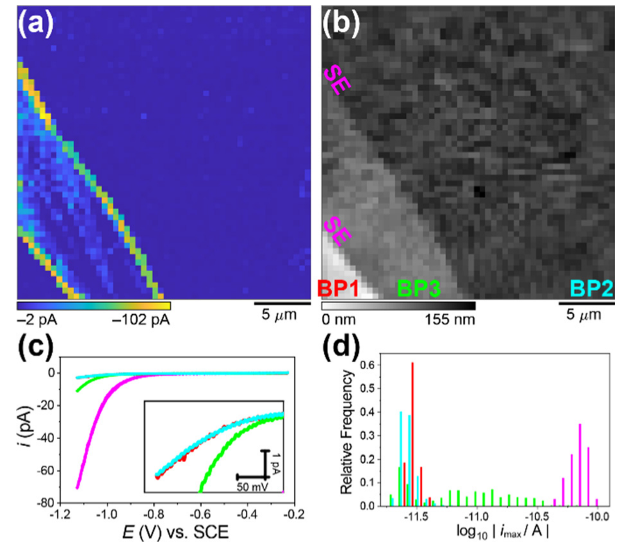

Fig. 1 Spatially-resolved maps of (a) i_{max} (extracted at −1.13 V *vs.* SCE, full i–E data available in ESI,† Movie S1) and (b) topography, obtained from the surface of bulk 2H-MoS_2. (c) Mean LSVs (voltammetric scan rate, υ = 1 V s^{-1}) and (d) normalised histograms of i_{max}, extracted from the corresponding regions marked in (b). Inset in (c) is a zoomed-in view of the LSVs obtained from BP1, BP2 and BP3. The SECCM probe contained 0.1 M $HClO_4$. Tip radius, tip area and hopping distance were ∼0.067 μm, ∼0.014 μm^2 and 0.5 μm, respectively. BP = basal plane; SE = step edge.

cannot indicate on the relative surface roughness of the BP areas, which are expected to be atomically smooth based on previous correlative AFM imaging.[6]

BP1 and BP2 both appear to possess relatively uniform electrocatalytic activities, while BP3 possesses significantly higher and more spatially-heterogeneous activity. Mean linear-sweep voltammograms (LSVs) extracted from the different regions, shown in Fig. 1c (pixel selection is detailed in the ESI,† Fig. S7), also further demonstrate the relatively high activity of BP3, with i_{max} values of −2.8, −2.8 and −11 pA measured at BP1, BP2 and BP3, respectively (*c.f.* −71 pA from the SEs). The abnormally high and spatially-heterogeneous activity of BP3 is further illustrated by constructing histograms of i_{max}, as shown in Fig. 1d. BP1, BP2 and the SEs all exhibit unimodal log-normal distributions, with mean ± standard deviation values of −11.57 ± 0.07, −11.55 ± 0.05 and −10.17 ± 0.08, respectively. On the other hand, BP3 exhibits a more complex $\log_{10}|i_{max}|$ distribution, with a low activity domain centred around −11.6 (akin to BP1 and BP2) and a broader, more drawn out (multi-modal) domain spanning the values of −11.5 to −10.2, with the upper limit corresponding to a catalytic current of −70 pA, comparable to what was measured on the SEs.

To understand the nature of the structure that is giving rise to the elevated and spatially-heterogeneous activity on BP3, scanning electron microscopy (SEM) was performed on the SECCM scan area (shown in the ESI,† Section S3 and Fig. S12). The feature of interest is shown in Fig. 2a, alongside co-located maps of topography (Fig. 2b) and electrochemical activity (Fig. 2c). Evidently, BP3 does appear to be different to BP1 and BP2 under SEM, showing prominent regions of light and dark contrast (Fig. 2a), which do not necessarily correspond to specific regions of low/high topography (Fig. 2b) or activity (Fig. 2c). Although the exact cause of the surface contrast in SEM is not known (seen in both secondary electron and backscatter electron detector modes, see ESI,† Fig. S12), it is likely attributable to local differences in electronic structure,[17] possibly induced by spatial variations in composition (*e.g.*, non-stoichiometric Mo : S ratios[18]) and/or surface topology (*e.g.*, mechanical straining of the BP[19,20]) on the sub-10 nm scale (*i.e.*, beyond the limit of detection for SECCM, herein). Changes in the local electronic structure may influence the free energy for adsorbed atomic hydrogen (ΔG_{H^*}), which is a widely-accepted descriptor for understanding the performance and further predicting the activity of HER electrocatalysts (*i.e.*, $\Delta G_{H^*} \approx 0$ eV for an "ideal" HER electrocatalyst).[1,2,21]

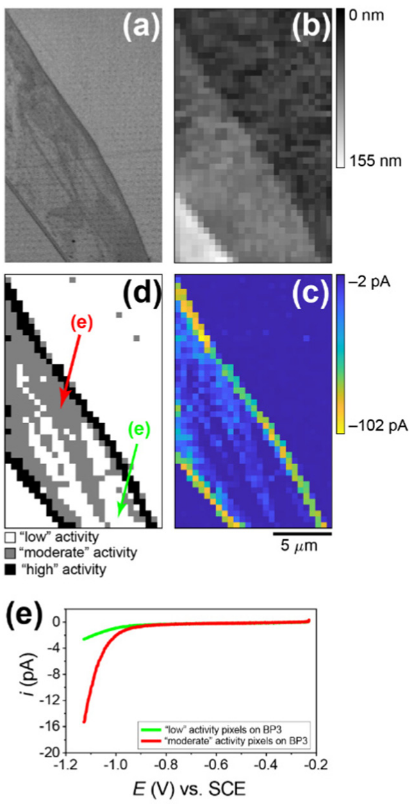

Fig. 2 Co-located (a) SEM image and zoomed-in maps of (b) topography and (c) i_{max}, obtained from the surface of 2H-MoS_2. (d) Trinarised image of $|i_{max}|$, where white, grey and black pixels represent: $|i_{max}| \le |1.5 \times i_{max,median}|$, $|1.5 \times i_{max,median}| < |i_{max}| \le |15 \times i_{max,median}|$ and $|i_{max}| > |15 \times i_{max,median}|$, respectively. (e) Mean LSVs (υ = 1 V s^{-1}) extracted from white (green trace) and grey (red trace) pixels of BP3, indicated in (d).

To separate the "low" and "high" activity regions (pixels) of BP3, the dataset were trinarised into three bins with respect to the median i_{max} ($i_{max,median}$ = −2.88 pA) in Fig. 1a. $|i_{max}| \le |1.5 \times i_{max,median}|$, $|1.5 \times i_{max,median}| < |i_{max}| \le |15 \times i_{max,median}|$ and $|i_{max}| > |15 \times i_{max,median}|$ were represented by white, grey and black pixels, respectively, as shown in Fig. 2d. Note that the lower and upper bin limits correspond to i_{max} values of −4.32 and −43.2 pA, respectively. In this simplified activity map (further details on this approach and justification of the

i_{max} boundary values are available in the ESI,† Section S1), it is quite evident that the regions of ''low'' (white pixels) and ''moderate'' (grey pixels) activity on BP3 are relatively localised and form contiguous, interweaved structures that are superficially similar in appearance to the contrasted structures observed in SEM (Fig. 2a). Separating the mean LSVs from these two regions (pixel selection shown in the ESI,† Fig. S8), shown in Fig. 2e, it is clear that the ''low'' activity region possesses a comparable activity to BP1 and BP2 (i_{max} = −2.6 pA), whereas the ''moderate'' activity region possesses an activity that is intermediate between the BP and EP (i_{max} = −15.3 pA). Also note that four pixels on the left of BP3 considered to be ''high'' activity (black in colour, Fig. 2d), indicating an EP-like ability to catalyse the HER at these sites.

In Fig. 2d, it is interesting to note that there are ''moderate'' activity pixels (grey in colour) located on BP2, well away from BP3 and the SE. Trinarising the entire scan area reveals clusters of these local electrocatalytic ''hot spots'' distributed over the entire surface of BP2, as shown in Fig. 3a. The two small clusters of red- and cyan-labelled pixels (bottom-right of Fig. 3a) coincide with distinct structures found on the MoS_2 surface with SEM (images shown in the ESI,† Fig. S12) that are too small to be identified in the SECCM topography map with a probe of this size (note that few-layer SEs on the order of 2–3 nm have previously been identified using probes of ∼30 nm diameter[6,10]). As shown in Fig. 3b, the red- and cyan-labelled features produce mean LSVs with i_{max} values of −8.2 and −6.1 pA, respectively (*c.f.* −2.8 pA over the entire surface of BP2). On the other hand, the green-labelled pixels scattered over the surface of BP2 (middle, top-left and top-right of Fig. 3a) do not correspond to any obvious features in the topography or SEM image and produce a mean i_{max} value of −4.8 pA (*ca.* double that of the pristine BP). This suggests that these electrocatalytic ''hot spots'', present at pixel and areal densities of ∼1.3% (≈ active pixels on BP2/total pixels on BP2) and ∼1 μm^{-2} [≈ active pixels on BP2/(total pixels on BP2 × tip area)], respectively, may correspond to individual defect sites in the pristine BP that happen to be present within the probed area of the SECCM droplet cell. Note that these ''hot spots'' remain more active for the duration of meniscus-surface contact (*e.g.*, during retract, see ESI,† Fig. S9), demonstrating that they are persistent on at least the ms to s timescale.

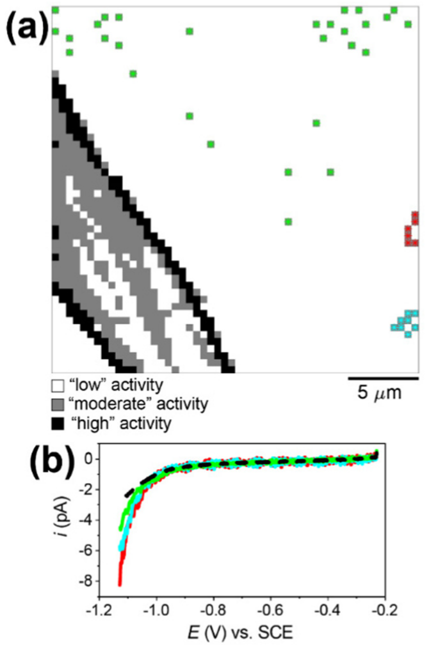

Fig. 3 (a) Trinarised image of $|i_{max}|$. (b) Mean LSVs (υ = 1 V s^{-1}) extracted from the corresponding green, red and cyan pixels, labelled in (a). The mean LSV extracted from the entire BP is also shown (black dashed line). Note that this is the same scan area that was reported in Fig. 1.

Single-defect sensitivity has previously been shown in SECCM, which has been used to probe nm-sized defects in chemical vapour deposition (CVD) graphene and MoS_2,[22,23] although this is the first time such an observation has been made in the context of HER electrocatalysis. The estimated areal density of electrocatalytic ''hot spots'', estimated above, is consistent with a previous scanning tunnelling microscopy study on natural molybdenite crystals, which reported areal defect densities that varied significantly from area-to-area (or crystal-to-crystal), within an estimated range of ∼0.1 to 10%, and corresponding to imperfections ranging in size from single-point defects (*e.g.*, sulfur vacancies) to gross structural defects (*e.g.*, pits).[24] It is also worth noting that introducing sulfur vacancies[19,20] and other gross defects[25] (*e.g.*, through introducing surface roughening[26] or porosity[27]) are well-known to enhance the macroscopic electrocatalytic activity of MoS_2 and related amorphous molybdenum sulfides, underpinning the important role of such structures as HER active sites.

To confirm the generality of this observation and experimental approach, additional SECCM scans were performed on entirely new bulk 2H-MoS_2 electrodes. An example of an electrochemical movie produced from one of the new scan areas is shown in ESI,† Movie S2. Consulting the i_{max} map produced from these data, Fig. 4a, the scan area is predominantly BP with a section of a large, multi-pixel SE feature captured in the bottom-left. Extracting the mean LSVs, Fig. 4b, the BP and SE possess similar activities to the scan area discussed above (Fig. 1–3), with i_{max} values of −2.7 pA and −72 pA, respectively. Trinarising the data, Fig. 4c, reveals two additional types of surface feature on the BP, which have been labelled with green (bottom-left) and magenta (distributed throughout) markers. The green-labelled pixels (Fig. 4c) are associated with the SE feature and produce a mean i_{max} value of −12.2 pA, as shown in Fig. 4d (comparable to the ''active'' pixels of BP3 in Fig. 1–3, discussed above). The magenta-labelled pixels (Fig. 4c) are distributed throughout the BP and produce a mean i_{max} value of −4.7 pA, as shown in Fig. 4d (*c.f.*, −4.8 pA for analogous sites in Fig. 3, above). These electrocatalytic ''hot spots'' are present at pixel and areal densities of ∼0.3% and ∼0.2 μm^{-2}, respectively, which is again within the range of defect densities previously reported for natural molybdenite crystals.[24] Also note that similar densities of electrocatalytic ''hot spots'' were also observed on an additional two 2H-MoS_2 crystals herein (ESI,† Fig. S10), as well as with previously published SECCM datasets[7,10]

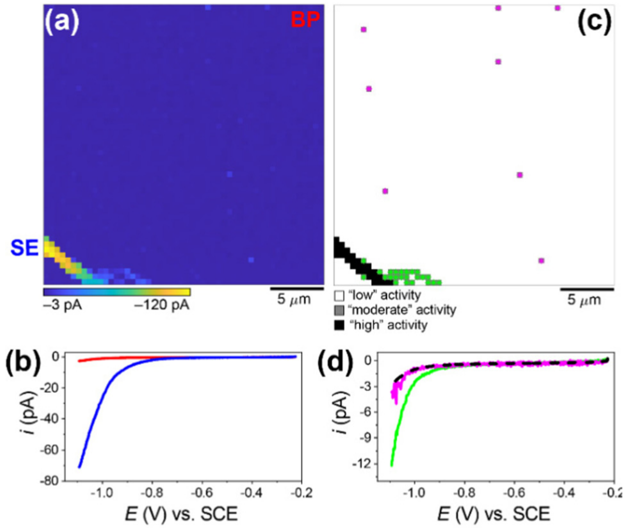

Fig. 4 (a) Spatially-resolved map of i_{max} (full i–E data available in ESI,† Movie S2), obtained from the surface of 2H-MoS$_2$. (b) Mean LSVs (υ = 1 V s^{-1}) extracted from the corresponding regions marked in (a). (c) Trinarised image of $|i_{max}|$. (d) Mean LSVs (υ = 1 V s^{-1}) extracted from the corresponding green and magenta pixels, labelled in (c). The mean LSV extracted from the entire BP is also shown (black dashed line).

(ESI,† Fig. S11) when subjected to the new data processing protocols (*i.e.*, data binning and trinarisation), reported herein.

In summary, SECCM has been employed to directly visualise previously unseen regions of high electrocatalytic activity on the BP of natural molybdenite (2H-MoS$_2$) crystals. Contiguous, μm-scale structures with local HER activities approaching that of the EP were shown to correspond to regions of contrast from co-located SEM imaging, and were attributed to variations in the electronic structure of the BP caused by local compositional and/or topological differences. Sub-μm electrocatalytic "hot-spots" were revealed through trinarising the spatially-resolved electrochemical data taken on four different MoS$_2$ crystals, and were attributed to the presence of individual defect sites present on the pristine BP surface. To further understand the nature of these electrochemical "hot spots", future studies will focus on employing different redox mediators (*e.g.*, $[Ru(NH_3)_6]^{3+/2+}$ and $[Fe(CN)_6]^{3-/4-}$, as in ref. 28) or passivating agents that target (passivate) specific types of defect (*e.g.*, sulfur vacancies[29]). Overall, this work further illustrates the strong potential of SECCM for structure–activity studies in electromaterials science, directly revealing the unique electrochemical activities of microscopic surface regions and rarer nanoscopic surface sites that may otherwise be overlooked when employing conventional "bulk" electrochemistry techniques alone.

CLB (project number: DE200101076) and MK (project number: DE220101105) are the recipients of an Australian Research Council (ARC) Discovery Early Career Researcher Award (DECRA), funded by the Australian Government. The authors acknowledge the use of the instruments and scientific and technical assistance at the Monash Centre for Electron Microscopy (MCEM), a Node of Microscopy Australia.

Conflicts of interest

There are no conflicts to declare.

Notes and references

1 J. D. Benck, T. R. Hellstern, J. Kibsgaard, P. Chakthranont and T. F. Jaramillo, *ACS Catal.*, 2014, **4**, 3957–3971.
2 Z. W. Seh, J. Kibsgaard, C. F. Dickens, I. Chorkendorff, J. K. Nørskov and T. F. Jaramillo, *Science*, 2017, **355**, 146.
3 Q. Ding, B. Song, P. Xu and S. Jin, *Chemistry*, 2016, **1**, 699–726.
4 L. Zhang, J. Zhu, X. Li, S. Mu, F. Verpoort, J. Xue, Z. Kou and J. Wang, *Interdiscip. Mater.*, 2022, **1**, 51–87.
5 S. M. Tan, A. Ambrosi, Z. Sofer, S. Huber, D. Sedmidubsky and M. Pumera, *Chem. – Eur. J.*, 2015, **21**, 7170–7178.
6 C. L. Bentley, M. Kang, F. M. Maddar, F. Li, M. Walker, J. Zhang and P. R. Unwin, *Chem. Sci.*, 2017, **8**, 6583–6593.
7 B. Tao, P. R. Unwin and C. L. Bentley, *J. Phys. Chem. C*, 2020, **124**, 789–798.
8 Y. Takahashi, Y. Kobayashi, Z. Wang, Y. Ito, M. Ota, H. Ida, A. Kumatani, K. Miyazawa, T. Fujita, H. Shiku, Y. E. Korchev, Y. Miyata, T. Fukuma, M. Chen and T. Matsue, *Angew. Chem., Int. Ed.*, 2020, **59**, 3601–3608.
9 S. Schumacher, L. Madauß, Y. Liebsch, E. B. Tetteh, S. Varhade, W. Schuhmann, M. Schleberger and C. Andronescu, *ChemElectroChem*, 2022, **9**, e202200586.
10 C. L. Bentley, M. Kang and P. R. Unwin, *J. Am. Chem. Soc.*, 2017, **139**, 16813–16821.
11 M. E. Snowden, A. G. Güell, S. C. S. Lai, K. McKelvey, N. Ebejer, M. A. O'Connell, A. W. Colburn and P. R. Unwin, *Anal. Chem.*, 2012, **84**, 2483–2491.
12 N. Ebejer, A. G. Güell, S. C. S. Lai, K. McKelvey, M. E. Snowden and P. R. Unwin, *Annu. Rev. Anal. Chem.*, 2013, **6**, 329–351.
13 L. Cheng, R. Jin, D. Jiang, J. Zhuang, X. Liao and Q. Zheng, *Anal. Chem.*, 2021, **93**, 16401–16408.
14 E. Daviddi, L. F. Gaudin and C. L. Bentley, *Curr. Opin. Electrochem.*, 2022, **34**, 101006.
15 C. L. Bentley, J. Edmondson, G. N. Meloni, D. Perry, V. Shkirskiy and P. R. Unwin, *Anal. Chem.*, 2019, **91**, 84–108.
16 C.-H. Chen, L. Jacobse, K. McKelvey, S. C. S. Lai, M. T. M. Koper and P. R. Unwin, *Anal. Chem.*, 2015, **87**, 5782–5789.
17 Q. H. Wang, K. Kalantar-Zadeh, A. Kis, J. N. Coleman and M. S. Strano, *Nat. Nanotechnol.*, 2012, **7**, 699–712.
18 M. V. Erdewyk and J. B. Sambur, *ACS Appl. Mater. Interfaces*, 2022, **14**, 22737–22746.
19 H. Li, M. Du, M. J. Mleczko, A. L. Koh, Y. Nishi, E. Pop, A. J. Bard and X. Zheng, *J. Am. Chem. Soc.*, 2016, **138**, 5123–5129.
20 H. Li, C. Tsai, A. L. Koh, L. Cai, A. W. Contryman, A. H. Fragapane, J. Zhao, H. S. Han, H. C. Manoharan, F. Abild-Pedersen, J. K. Norskov and X. Zheng, *Nat. Mater.*, 2016, **15**, 48–53.
21 C. Tsai, K. Chan, J. K. Nørskov and F. Abild-Pedersen, *Surf. Sci.*, 2015, **640**, 133–140.
22 C. L. Bentley, M. Kang, S. Bukola, S. E. Creager and P. R. Unwin, *ACS Nano*, 2022, **16**, 5233–5245.
23 M. B. Cabré, A. E. Paiva, M. Velický, P. E. Colavita and K. McKelvey, *J. Phys. Chem. C*, 2022, **126**, 11636–11641.
24 R. Addou, L. Colombo and R. M. Wallace, *ACS Appl. Mater. Interfaces*, 2015, **7**, 11921–11929.
25 G. Ye, Y. Gong, J. Lin, B. Li, Y. He, S. T. Pantelides, W. Zhou, R. Vajtai and P. M. Ajayan, *Nano Lett.*, 2016, **16**, 1097–1103.
26 S. C. Lee, J. D. Benck, C. Tsai, J. Park, A. L. Koh, F. Abild-Pedersen, T. F. Jaramillo and R. Sinclair, *ACS Nano*, 2016, **10**, 624–632.
27 C. L. Bentley, R. Agoston, B. Tao, M. Walker, X. Xu, A. P. O'Mullane and P. R. Unwin, *ACS Appl. Mater. Interfaces*, 2020, **12**, 44307–44316.
28 M. Velicky, M. A. Bissett, P. S. Toth, H. V. Patten, S. D. Worrall, A. N. J. Rodgers, E. W. Hill, I. A. Kinloch, K. S. Novoselov, T. Georgiou, L. Britnell and R. A. W. Dryfe, *Phys. Chem. Chem. Phys.*, 2015, **17**, 17844–17853.
29 H. Lu, A. Kummel and J. Robertson, *APL Mater.*, 2018, **6**, 066104.